



Multiscale hierarchical structures from a nanocluster mesophase

Haixiang Han^{1,8}, Shantanu Kallakuri ¹, Yuan Yao¹, Curtis B. Williamson², Douglas R. Nevers², Benjamin H. Savitzky³, Rachael S. Skye¹, Mengyu Xu¹, Oleksandr Voznyy ¹, Julia Dshemuchadse ¹, Lena F. Kourkoutis ^{5,6}, Steven J. Weinstein ¹, Tobias Hanrath ² and Richard D. Robinson ¹

Spontaneous hierarchical self-organization of nanometre-scale subunits into higher-level complex structures is ubiquitous in nature. The creation of synthetic nanomaterials that mimic the self-organization of complex superstructures commonly seen in biomolecules has proved challenging due to the lack of biomolecule-like building blocks that feature versatile, programmable interactions to render structural complexity. In this study, highly aligned structures are obtained from an organic-inorganic mesophase composed of monodisperse Cd₃₇S₁₈ magic-size cluster building blocks. Impressively, structural alignment spans over six orders of magnitude in length scale: nanoscale magic-size clusters arrange into a hexagonal geometry organized inside micrometre-sized filaments; self-assembly of these filaments leads to fibres that then organize into uniform arrays of centimetre-scale bands with well-defined surface periodicity. Enhanced patterning can be achieved by controlling processing conditions, resulting in bullseye and 'zigzag' stacking patterns with periodicity in two directions. Overall, we demonstrate that colloidal nanomaterials can exhibit a high level of self-organization behaviour at macroscopic-length scales.

he spontaneous self-organization of nanoscale materials into complex macroscopic architectures has intrigued scientists for decades, because it offers insight into how complex structures can emerge from primitive building blocks¹⁻⁴. Hierarchical self-assembled systems offer structural advantages that are absent in isolated constituent units^{5,6}. Nature is replete with fascinating examples of hierarchical assembly, such as proteins or DNA, and natural photonic structures as seen in butterfly wings or fish^{7,8}. Biosystems also invoke error-correction and defect tolerance in structures; together, these attributes provide a strong inspiration to create hierarchical systems from synthetic building blocks that nature has not yet had the opportunity to work with^{9,10}. Although synthetic materials that afford the same level of accuracy and complexity as biomolecules are currently beyond reach, research into the self-organization of artificial units has increased dramatically^{5,11,12}. Organic molecules and copolymers are among the most commonly used elementary units to form large-area patterning^{13–15}. More recently, advances in nanomaterial synthesis have provided access to a versatile library of nanoparticle building blocks with tunable composition, morphology and atomic structure that give rise to physiochemical properties unattainable in naturally occurring materials^{16,17}.

Beyond the formation of basic superstructures such as cubic close-packed assemblies, the creation of complex superstructures via nanoparticle assembly presents a persistent challenge. The most straightforward organization routes are through evaporative packing into well-structured superlattices^{18,19} and self-organization through surfactant–molecular linking (for example, DNA or RNA)^{20–22}. The resulting superlattice crystals, however, typically have domain sizes smaller than millimetres, are connected with noncomplex linkages

that result in simple organizations and are limited in tunability and continuity.

To achieve high-level, complex hierarchical assembly structures, colloidal nanocrystals that are small in size (<2 nm) and with a high ligand:core ratio may be used. Nanocrystals of this size invoke 'softer' interparticle interactions that yield a richer phase diagram beyond the classical close-packed structures seen with larger particles²³. For nanomaterials with scales approaching molecular complexes (for example, metal soaps), the intrinsic mesophase behaviour imparted by fatty acid ligands surrounding the inorganic core plays a critical role²⁴. Examples include mesophases that contain (CdSe)₁₃ nanoclusters between double-lamellar assemblies³, and long-range ordered superstructures from (CdSe)₁₃ and (ZnSe)₁₃ nanoclusters, which display high luminescence and catalytic activities²⁵. We previously reported an ultra-small, oleic acid-capped CdS magic-size cluster (MSC) that assembles into hexagonal mesophase filaments with nanometre spacing between MSC units both radially and axially²⁴.

Here, we report on the remarkable hierarchical assembly behaviour of these MSC nanomaterials with structural alignment that spans over six orders of magnitude in length scale! The 1.5 nm MSCs, the primary structure, are assembled into filaments that are micrometres in length and hundreds of nanometres in width (the secondary structure). These filaments align in a shear flow field which subsequently leads to the formation of band textures that uniformly span the centimetre-scale film. The hierarchical structures share intriguing similarities with band textures in liquid crystals; however, the presence of an inorganic MSC core with strongly quantum confined optoelectronic properties 4.26 introduces new possibilities to advance a new class of programmable optical metamaterials. We examine the fundamental processing-structure-property

¹Department of Materials Science and Engineering, Cornell University, Ithaca, NY, USA. ²Robert F. Smith School of Chemical and Biomolecular Engineering, Cornell University, Ithaca, NY, USA. ³Department of Physics, Cornell University, Ithaca, NY, USA. ⁴Department of Physical and Environmental Sciences, University of Toronto Scarborough, Toronto, Ontario, Canada. ⁵Kavli Institute for Nanoscale Science, Cornell University, Ithaca, NY, USA. ⁶School of Applied and Engineering Physics, Cornell University, Ithaca, NY, USA. ⁷Department of Chemical Engineering, Rochester Institute of Technology, Rochester, NY, USA. ⁸Present address: School of Materials Science and Engineering, Tongji University, Shanghai, China. [™]e-mail: th358@cornell.edu; rdr82@cornell.edu

relationships and propose a formation mechanism that intertwines microscopic phase behaviour with the macroscopic behaviour of receding liquid films during drying. The multiscale, self-organizational behaviour demonstrated in these MSC films shows a potential new pathway to organize and study complex mesoscopic and mesoscopic structure.

Results

Length scales of hierarchical self-organization. Ultrapure CdS MSCs were synthesized at high yield through our previously reported high-concentration synthetic method²⁴. The atomic structure of MSCs can be formulated as Cd₃₇S₁₈, with the core Cd atoms being coordinated with S in a tetrahedral geometry normally seen in bulk extended solids (Fig. 1e, inset) but with an overall low-symmetry molecular structure due to their ultra-small size4. Dissolving CdS MSCs in non-polar solvents like hexanes increases the viscosity of the MSC solutions nonlinearly with concentration, which we attribute to changes in the phase behaviour²⁴. Polarized optical microscopy (POM) imaging of MSC solutions reveals concentration-dependent phase transition behaviour as evidenced by distinguishable textures characteristic of lyotropic liquid crystals (Supplementary Fig. 7). Controlled evaporation of the solvent leads to the formation of highly ordered films. For example, long-range ordered thin film structures can be formed through controlled solvent evaporation from a concentrated 20 mg ml⁻¹ solution. Periodic structures align into centimetre-scale superstructures (Fig. 1a). The high uniformity of the transmission and reflection diffraction patterns reveals extraordinary structural fidelity without any obvious defects or discontinuities in surface texture (Supplementary Figs. 8 and 9). Structural fidelity was confirmed via optical microscopy (OM) of various regions of a sample. Millimetre-scale OM images show continuous striped patterns with distinct spots in the corresponding fast Fourier transform, indicating a high level of periodicity (Fig. 1b). The grating formed by the highly aligned bands—the quaternary level structure—is responsible for the centimetre-scale rainbow reflection seen in Fig. 1a. Higher-magnification OM images show highly aligned band patterns (Fig. 1c, left) for films dried under controlled evaporation, and randomly oriented textures (Fig. 1c, right) formed under ambient conditions—that is, with neither the evaporation geometry nor the timing of solvent evaporation controlled. These larger, macroscopic bands represent a tertiary structure in the hierarchical self-assembly process. Higher-magnification transmission electron microscopy (TEM) images reveal the filamentous subunits (Fig. 1d) that make up the ordered bands of the secondary-level structure. The filaments isolated were obtained and imaged after disentangling them by dilution (1 mg ml⁻¹ in hexane solvent) and sonication (10 min), emphasizing their propensity to tangle into larger structures. MSC filaments are structurally robust and persist even after prolonged sonication or under dilute conditions, indicating the presence of a relatively strong interaction force between proximate MSCs that cannot be disrupted by simple mechanical vibrations. The structural characteristics of MSC filaments are reminiscent of a mesogen, which usually contains a rigid core structure and flexible tails that enable the formation of a liquid crystalline phase (Supplementary Fig. 10)27. At the nanometre scale, annular dark-field high-resolution scanning TEM (STEM) shows that aligned MSCs are the foundational-level (primary structure) building blocks of the filaments (Fig. 1e). Within each filament, MSCs are ordered through an 'organic-inorganic mesophase'24 that is a direct product of the synthesis. This ordered, three-dimensional (3D) assembly was established in our previous investigation through small-angle X-ray scattering (SAXS). The SAXS profile indicates that MSCs arrange in a hexagonal geometry with 3.4 nm d-spacing along the radial direction (Supplementary Fig. 12) that is probably determined by partially interdigitated oleate ligand shells. The radial grain size is >170 nm (ref. 24).

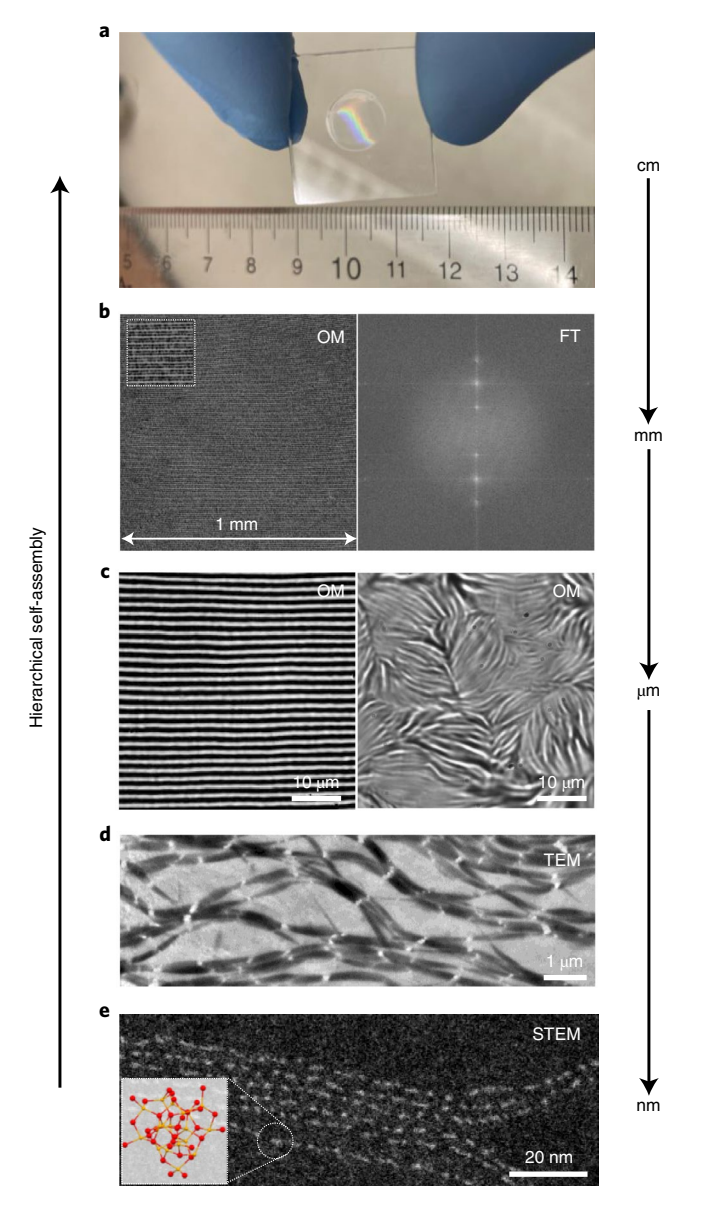


Fig. 1 | Hierarchical self-assembly of 1.5 nm MSCs into centimetre-scale aligned bands. a, Solid thin film prepared by evaporation-driven self-assembly of 20 mg ml⁻¹ MSC solution. The as-prepared thin film reflects rainbow colours in centimetre-scale patterns, illustrating emergent optical properties arising from the highly periodic surface texture. **b**, Left: OM image and (inset) higher-magnification image of the thin film shown in **a**, revealing millimetre-scale surface periodicity; right: corresponding Fourier transform (FT). **c**, Higher-magnification OM images of highly aligned bands (left) and random orientated film (right) formed from MSC cables. **d**, TEM image of the filament subunit structure. **e**, Annular dark-field, high-resolution STEM images of nanofilaments formed from self-organization of 1.5 nm CdS MSCs, which appear as bright spots. Atomic structure of the Cd₃₇S₁₈ MSC (inset).

Axially, the mesophase filament length is in the order of tens of micrometres. While the nanofilaments are the direct product of synthesis²⁴, the higher-level structures are constructed from these nanofilaments during the evaporation process. MSCs have an anisotropic morphology with a prolate shape along the filament length (Fig. 1e).

Based on the structure of individual MSCs⁴, their secondary assemblies (filaments)²⁴ and the nature of interaction forces²⁸,

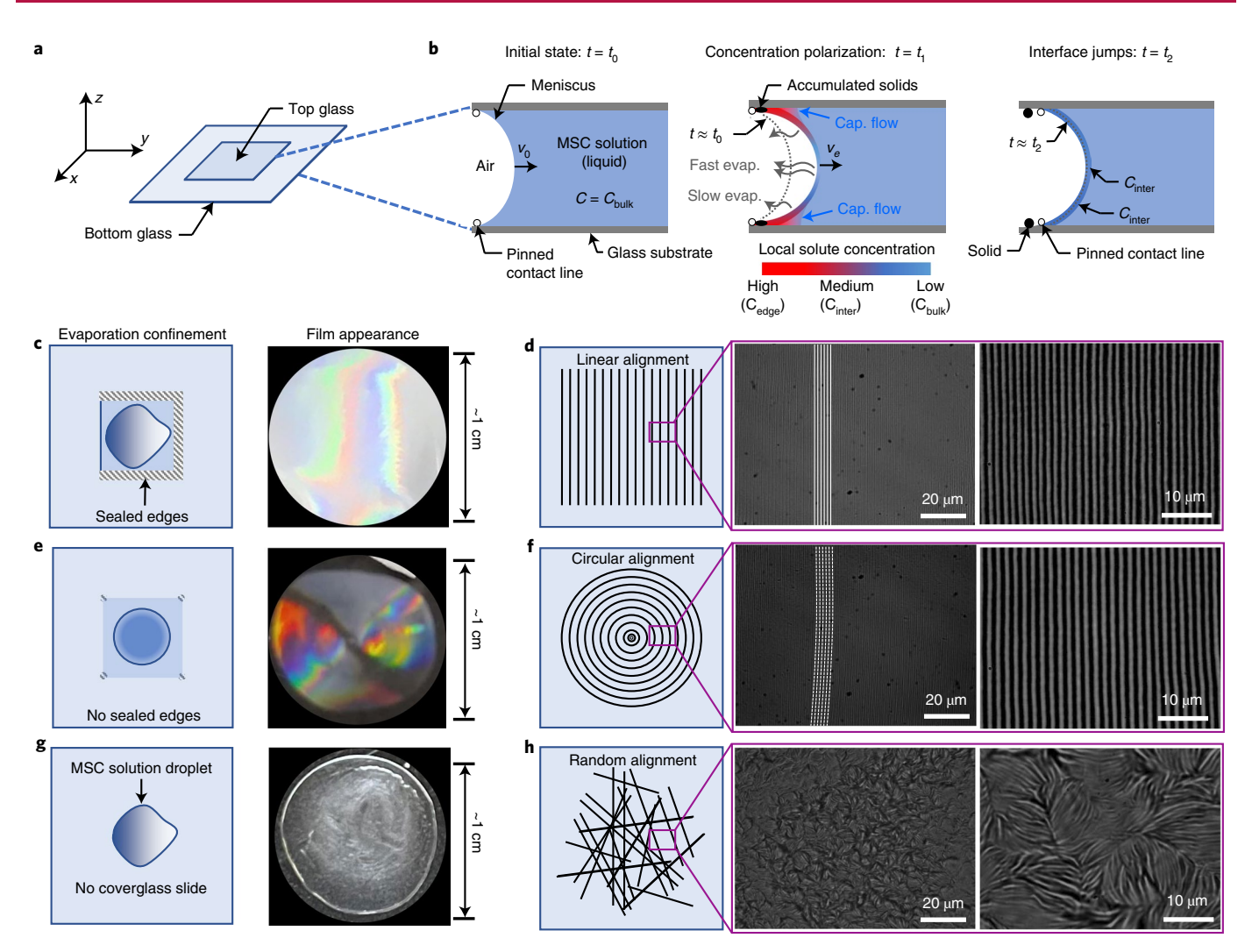


Fig. 2 | Method and mechanism for patterning of aligned films using different geometric confinements. a, Schematic of experimental setup for preparation of thin films from CdS MSC solution. Two glass slides are separated by a thin gap (\sim 100 µm) filled with MSC solution. **b**, Schematic of thin film formation mechanism during solvent evaporation (evap.). *t* is time, where t_0 is time zero and t_1 and t_2 are subsequent times; V_0 is the initial velocity; C is concentration, where C_{bulk} is the bulk concentration, C_{inter} is an increased concentration of dispersed solid near the interface, and C_{edge} is a much higher concentration of solids that continue to accumulate near the pinned contact line; and Cap. flow is capillary flow. Full model details can be found in the Supplementary Information. **c**, Left: schematic illustrating the experimental setup for linearly aligned thin film patterns; right: photograph of the film reflecting linearly aligned rainbow colours under visible light. **d**, Schematic and OM images of thin film prepared using the method shown in **c**. Unidirectional solvent evaporation results in a film with aligned bands oriented parallel to the evaporation front. The pattern is enhanced with highlighting in the left-hand OM image. **e**, Left: schematic illustrating the experimental setup for bullseye thin films; right: photograph of thin film reflecting circularly aligned rainbow colours under visible light. **f**, Schematic and OM images of thin film prepared using the method shown in **e**. The pattern is enhanced with highlights in the left-hand OM image. **g**, Left: schematic illustrating the experimental setup for randomly oriented thin films by drop-casting of MSC solution onto a glass slide; right: photograph demonstrating that the film does not reflect a colour spectrum due to the lack of surface periodicity. **h**, Schematic and OM images of thin film prepared using the method shown in **g**, containing randomly oriented cables.

there are probably several driving forces for cluster–cluster linkages. The prolate shape of the MSC, the non-spherical ligand shell and thermal distortions induce a dipole (\sim 7–20 D; Supplementary Information), which aids in aligning neighbouring MSCs through dipole–dipole interaction in a 'head-to-tail' alignment. For colloidal nanocrystals capped with surfactant ligands having a long hydrocarbon chain (C_{12} – C_{18}), the two neighbouring nanocrystals can be linked through packing of parallel, head-to-tail ligands, which has been modelled by Schapotschnikow and Vlugt²⁹. In addition, intermolecular interactions between oleates, like van der Waals forces, are possibly involved in the ligand–ligand interactions into larger fibres³², which contain multiple filament subunits

(Supplementary Fig. 10). Depending on the processing regime, the filaments align along the meniscus front, forming alternating ridges (stick region) and troughs (slip region) that are perpendicular to the evaporation direction, through a stick-and-slip process, or they form via a relax-and-recoil mechanism commonly observed in liquid crystals wherein the filaments align in the direction of shear from the receding meniscus and subsequently buckle as the internal elastic energy of the fibre relaxes mechanically³³.

Pattern formation method and mechanisms. To better understand and ultimately control the processing–structure relationships governing evaporation-driven assembly, we examined macroscopic film formation via controlled evaporation experiments in defined

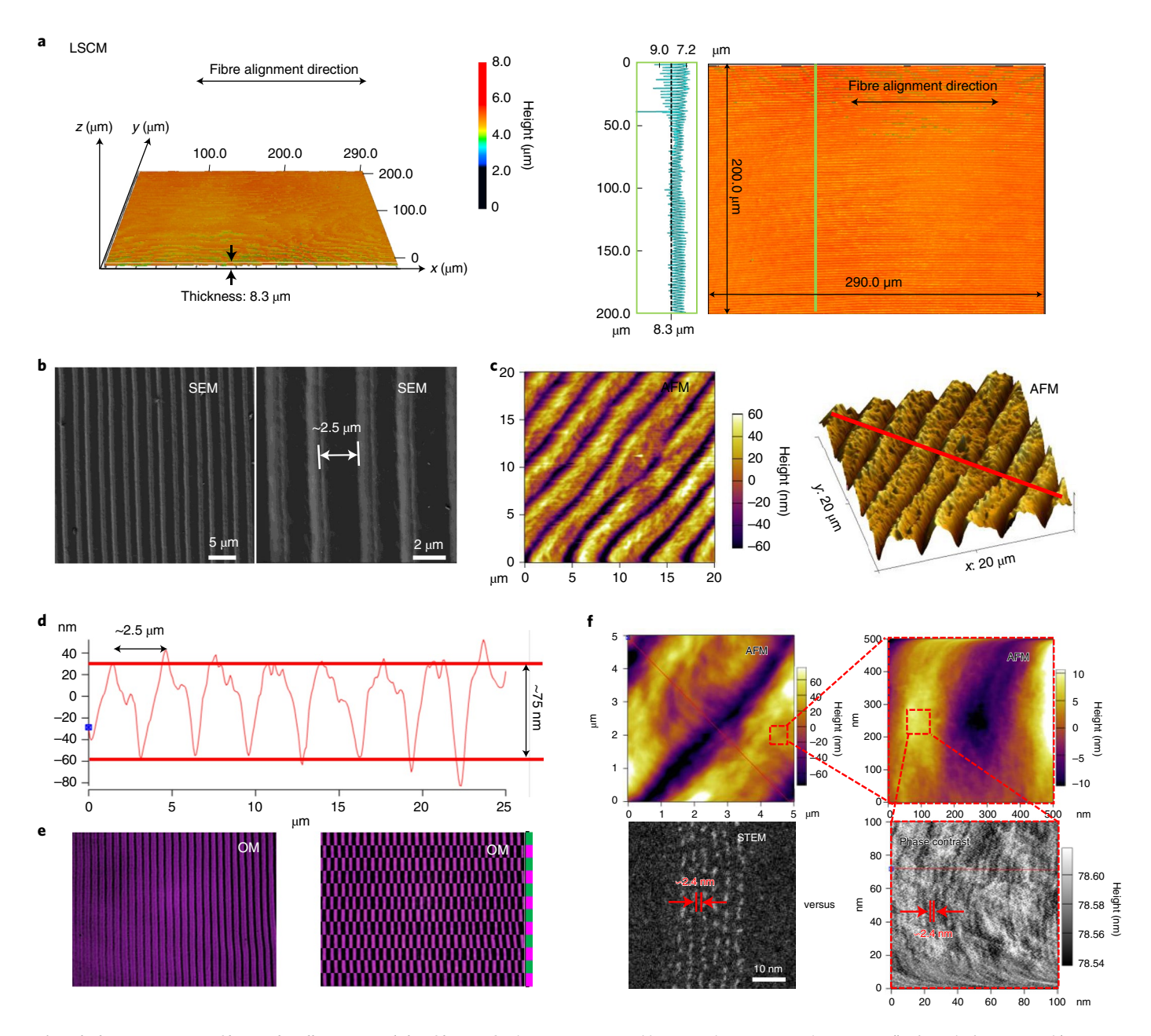


Fig. 3 | Characterization of hierarchically patterned thin films. a-f, Films were prepared by natural evaporation (-0.06 μm s⁻¹) of 30 μl of a 20 mg ml⁻¹ MSC solution in a two-glass configuration with a -100 μm gap and three edges sealed, as shown in Fig. 2c. **a**, LSCM of the thin film surface profile shows an average thickness of -8.3 μm and a surface texture with long-range periodicity. **b**, SEM images of the thin film. **c**, Low-magnification AFM images of the thin film d, Surface profile of the thin film extracted using AFM microscopy (red line). **e**, Left: optical images of the thin film; right: two optical images of the thin film taken at different focal planes and stitched together. **f**, High-magnification AFM and corresponding phase images of the thin film compared with the high-magnification, annular dark-field STEM image.

geometries on glass slides. The highest-quality bands were achieved using a simple two-glass configuration with a $\sim\!100\,\mu m$ gap between the slides and three edges sealed (Fig. 2a–d); Detailed aspects of the formation mechanism and the relationship between shear and drying phenomena and the resulting film texture are discussed in the Supplementary Information. For the banded assemblies, a simplified assembly mechanism to estimate the wavelength of the deposits yielded values consistent with experimental results (Fig. 2b and Supplementary Information). This geometry confines the evaporation direction and reduces evaporation rate. As the MSC solution ($\sim\!40\,\mu$ l) evaporates, an air gap ($\sim\!84\,\mu$ m) forms between slides (Supplementary Figs. 13 and 14) and two nearly identical

(same thickness and pattern) thin films are formed on both slides (Supplementary Fig. 15). When the evaporation is confined to a single direction, the films show a highly aligned linear pattern with the bands oriented parallel to the drying front. Optical microscopy images show a periodic arrangement of straight bands (Fig. 2d) with a periodicity of ~2.5 μ m. The film exhibits minimal thickness variations at the centimetre-length scale and displays a rainbow colour across the full ~1 cm length of the dried film (Fig. 2c, right). This coloration is caused by diffraction of incident light reflecting off the periodically ordered array of bands (Supplementary Information)³⁴. Along with the films' transmissive diffraction properties (vide infra), this chromatic grating effect underscores the high degree of

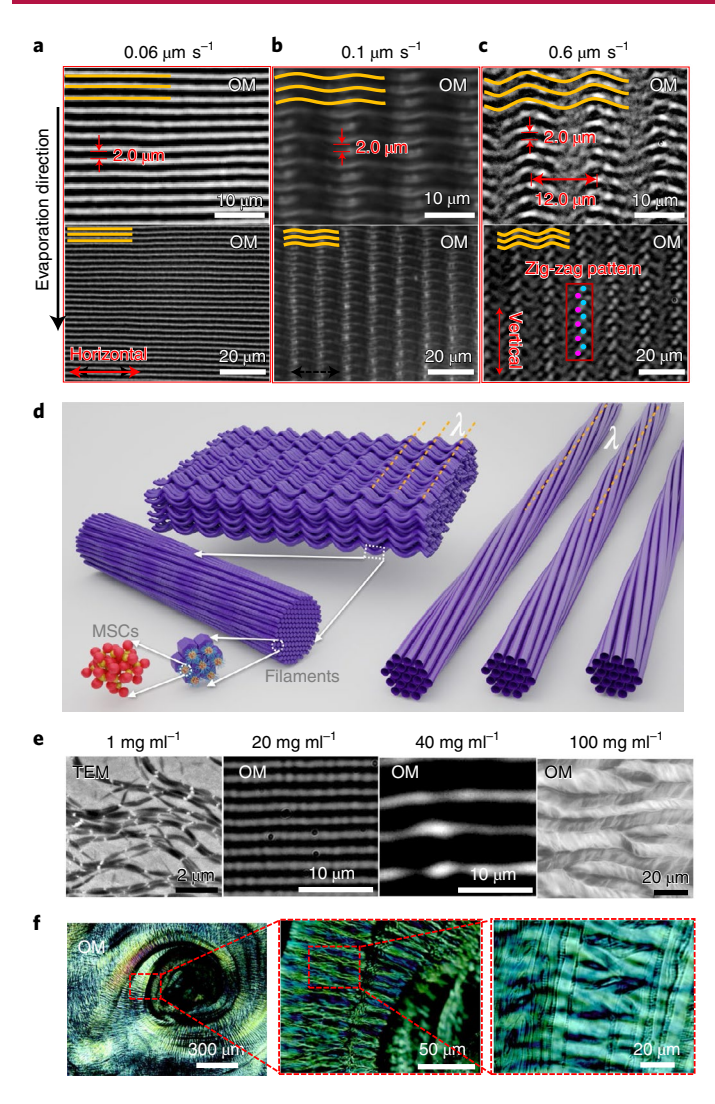


Fig. 4 | Tuning of thin film morphology through solvent evaporation rate and concentration. a–c, Optical microscopy images of thin films prepared at different evaporation rates: $0.06 \,\mu\text{m}\,\text{s}^{-1}$ (**a**), $0.1 \,\mu\text{m}\,\text{s}^{-1}$ (**b**) and $0.60 \,\mu\text{m}\,\text{s}^{-1}$ (**c**). **d**, Schematic illustrating the self-assembly process from MSCs to filaments to bands, and the increased complexity arising from twisted units. **e**, TEM and OM images of MSC filaments and bands prepared from MSC solution at different concentrations. The concentration sequence is used to demonstrate structures that form at different stages of the self-assembly process. **f**, OM images of patterns formed by spin-coating MSC solutions. Enlarged images show similar helical units.

structural uniformity in the spacing and orientation of bands within the thin film. Aside from mechanistic insights, these findings also have important technological implications because they underscore the ability to define band alignment in the thin film by geometrical constraint of the orientation of the receding evaporation front.

We examined a series of geometries to impose the assembly direction and test the extent to which the resulting patterns can be controlled. When the geometry is modified as two glass slides with all edges unsealed, creating a radial evaporation front, the orientation of the bands continues to be parallel to the drying front, thereby producing a bullseye-like thin film (Fig. 2e,f and Supplementary Figs. 18 and 19). Enlarged OM images (Fig. 2f) show band patterns with ~2.5 µm spacing, similar to those seen in the three-sides-confined geometry (Fig. 2d) but with a slight curvature. A low-magnification view of the film shows the coloured diffraction pattern expected for a circular pattern (Fig. 2e, right, and

Supplementary Fig. 20). Control experiments without a top coverslide and without controlled evaporation did not produce ordered patterns (Fig. 2g,h). The resulting films have an uneven thickness, with curved morphology (thicker middle) and turbulent surface texture. Optical microscopy reveals randomly oriented textures mostly parallel to the glass substrate and have the same feature size as the periodic bands, implying a connection with the constituent units that make up the band features (Fig. 2h and Supplementary Fig. 19). Due to the lack of alignment, the thin film appears cloudy and white with a rough surface (Fig. 2g, right).

Using topographical characterization methods, we confirm that the periodicity and thickness of the films are in the micrometre range. Laser scanning confocal microscopy (LSCM) affords quantitative analysis for the surface profile of the thin film over a relatively large lateral area (290×200 μm²). The average thickness of a film made from a concentrated ($20 \,\mathrm{mg}\,\mathrm{ml}^{-1}$) solution is $8.3 \pm 0.9 \,\mu\mathrm{m}$ (Fig. 3a, left), with a surface texture similar to that seen under OM. A line profile perpendicular to the surface texture (orthogonal to the bands) measures a sinusoidal pattern with 2.5 µm periodicity (Fig. 3a, right), confirming the high level of uniformity measured with other characterization methods. It should be pointed out that the profile of the thin film is independent of gap spacing between the two confining glass slides: when the gap is increased to 200 µm, the films maintain a relative thickness of 8.5 µm. The thickness of the thin films, however, is dependent on concentration: thickness increases to $\sim 14 \, \mu m$ at a concentration of $40 \, mg \, ml^{-1}$. Focusing on a smaller area, scanning electron microscopy (SEM) images show aligned bands with 2.5 µm spacing (Fig. 3b) while higher-magnification images reveal small fibrous fine structure on each band, resembling wrapped strands in a rope (Fig. 3b, right, and Supplementary Fig. 23). The diameter of the small fibrous feature is ~300 nm, matching the size of the filaments (Fig. 1d) and confirming that filament units are the substructures of the larger bands. The atomic force microscopy (AFM) characterization and line profile confirms the 2.5 µm spacing between bands and reveals a peak-to-valley height amplitude of ~75 nm (Fig. 3c,d). The topography and fine structure of the MSC bands share several similarities to those found in liquid crystals³⁵. Varying the focal depth of the optical microscope leads to systematic shifts in the band textures (Supplementary Video 1), which suggests the existence of additional film structure in the vertical direction. Paired bands can be seen with microscope images taken where the focal plane is set to the middle point of the paired bands, making the pattern lines broader with a central ridge (Fig. 3e, left). Clearer images of the two-level structure can be created by superimposing two focused images from each of the two layers, clearly exhibiting a stacking step pattern with the bands (Fig. 3e, right). The phase image from high-magnification AFM microscopy on a nanoscale region $(100 \times 100 \text{ nm}^2; \text{ Fig. 3f})$ of the thin film reveals the presence of aligned valleys with 2.3 nm spacing. This is comparable to the distance between the chains of MSCs obtained from the high-resolution STEM image (Fig. 3f, lower left). Therefore, the solidified thin film still contains the secondary structure from the solution-phase MSCs, indicating a hierarchical structure down to the MSC mesophase.

Tuning and behaviour of film morphology. In addition to in-plane tunability (that is, circular versus linear configuration), out-of-plane periodic features can be created by accelerating the evaporation rate (Supplementary Fig. 24). As discussed above, the natural evaporation rate ($\sim 0.06 \, \mu m \, s^{-1}$) results in aligned and parallel bands forming the long-range order of a grating (Fig. 4a). Decreased evaporation rates ($\sim 0.003 \, \mu m \, s^{-1}$) do not significantly change the band patterning (Supplementary Fig. 25). On the contrary, increased evaporation rates form out-of-plane wave features on the in-plane pattern. Specifically, at an evaporation rate of $0.1 \, \mu m \, s^{-1}$, the films have the primary band structure

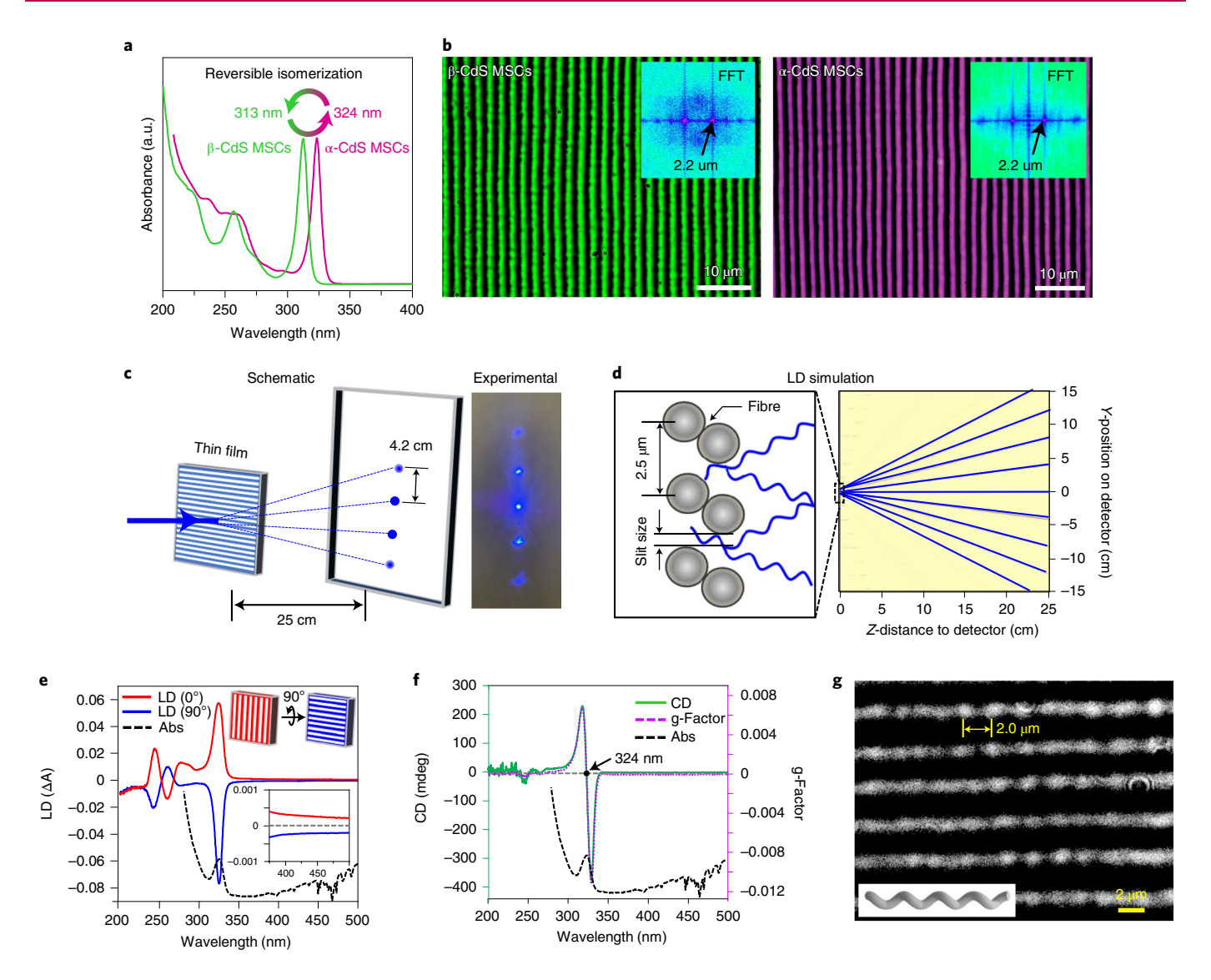


Fig. 5 | Optical properties of thin films. a, Absorption spectra for thin film treated with methanol vapour, following which the characteristic absorption peak changed from an initial 324 nm to 313 nm, while after methanol removal by gentle heating at 60 °C for 30 min, the absorption peak shifted back to 324 nm. The entire process can be repeated and is reversible. **b**, Comparison of OM images of the thin film before (left) and after treatment (right) with methanol vapour. Images show that the overall texture of the thin film remained identical throughout the isomerization process of constituent MSCs. **c**, Laser diffraction experiment on thin film. **d**, Simulated laser diffraction pattern distribution. **e**, LD spectra of the thin film at sample alignment of 0° (red) and 90° (blue) to the orientation axis. Inset shows LD spectra for wavelength range 350–500 nm. Abs is the absorption spectrum, shown in black. ΔA is the difference in absorption between light polarized parallel and perpendicular to an orientation axis. **f**, CD spectrum and g-factor of the thin film. mdeg is the measure of ellipticity in millidegrees; g-factor is ellipticity divided by the absorbance (Abs). **g**, OM image of the thin film showing the helical morphology of cables. a.u., arbitrary units.

(with ~2.5 μm wavelength) and an additional orthogonal band structure with a wavelength of ~10 μm (Fig. 4b). Increasing the evaporation rate to $0.6\,\mu m$ s $^{-1}$ further offsets this distortion (Fig. 4c and Supplementary Figs. 26–28), which gives rise to 'zigzag' stacking patterns. This result aligns well to previous work on assemblies of bacteriophages that found band structures at low pulling speeds and complex patterning similar to ours at high speeds 36 . To investigate more fully the influence of evaporation rate on band morphology, we used initial preparation conditions as for the films shown in Fig. 3 then performed an in situ experiment where the evaporation rate was dynamically altered and accelerated by application of a small vacuum (Supplementary Fig. 29 and Supplementary Table 1). As can be seen in the images, a slow evaporation rate forms linear periodic bands but at faster evaporation speeds the instabilities produce two-dimensional periodic

structures that have additional wave-like features. Using speeds estimated from our in situ optical videos, the cross-over point was found to be $\sim 0.08\,\mu m\,s^{-1}$. Evaporation rates faster than this lead to inhomogeneities of the linear bands (Supplementary Fig. 25). Previous work has reported that patterning of a polymer film can be controlled by tuning the evaporation rate 33,37 . We speculate that the higher-order textures result from the relaxation of additional stresses introduced by the faster solvent evaporation rate, transitioning the formation mechanism from a stick-and-slip deposition to one where shear forces can cause alignment in two directions. Whereas the mechanistic details responsible for the formation of the higher-order band textures are not yet clear, we see the ability to control complex band textures with orthogonal orientations as an attractive experimental degree of freedom for future exploration of these films as programmable optical metamaterials.

The current study demonstrates that 1.5 nm CdS MSC colloidal nanomaterials can exhibit complex self-organization patterns without the use of biomolecules as surfactant ligands (Fig. 4d). CdS MSCs, the primary structural level, assemble into a secondary structure of filaments with hexagonal geometry at a periodic radial spacing of 3 nm, as we previously reported24. The higher levels of structure can be teased apart by changing the concentration of the mesophase solution (Fig. 4e and Supplementary Fig. 30). Diluting the MSC solution to 1 mg ml⁻¹ allowed us to examine the structure of isolated filaments by TEM (Fig. 4e, left); the filaments are typically ~300 nm wide and extend to ~10 µm in length. Each filament exhibits rope-like wrapping when forming the periodic band patterns (unwound bands shown in Supplementary Figs. 34 and 35). Increasing the MSC concentration solution to 100 mg ml⁻¹ produces yet another hierarchical level wherein thicker bands (~10 µm) exhibit additional fine structure evident within each band (Fig. 4e, right). These structures show high correspondence to band textures in mesomorphic polymers and liquid crystals where buckling is thought to lead to the band formation³⁷. Combining high concentrations with faster evaporation rates from fewer confined boundaries results in transitions from the simple band patterns into more complex structures (Supplementary Fig. 36). These results link well to the complex structures forming at high evaporation rates. Instead of a highly symmetric atomic lattice as commonly seen in larger nanoparticles (>2 nm)²⁶, our ultra-small CdS MSCs feature a molecular structure that, along with its organic ligand shell, probably has non-symmetric or chiral structural features that are amplified through the assembly process²⁴. This organization process is consistent with chiral amplification effects where the chirality from small motifs can be hierarchically amplified to form higher-level structures. Micrometre-sized filaments can be recovered from banded thin films by redissolving solid films in hexanes. Conversely, experiments employing MSCs without mesophase filaments showed no formation of macroscopic-length bands.

In the stick-and-slip regime, it is possible that, to increase their stability, multiple filaments self-organize around each other as they assemble into bands (Fig. 4d). The band widths are nearly monodisperse, which may be explained by the balance between the strain energy of twisting and the energy reduction on assembly (Supplementary Information)^{38,39}. Spin-coating of MSC solutions results in spiral patterns that retain the aspects of the band texture (Fig. 4f). As found in high-concentration films with planar evaporation fronts (Fig. 4e), higher-magnification images in spin-coated samples reveal giant twisting cables composed of two twisted sub-cables (Fig. 4f). The variety of film morphologies in Fig. 4 indicates how MSC mesophases may be manipulated to achieve different complex patterns, which reveals a promising path for control of various structures in future work.

Optical properties. The emergent optical properties in hierarchical assemblies present intriguing scientific questions (Supplementary Information). Films are able to undergo reversible, chemically induced isomerization over multiple cycles without alteration of surface patterning²⁶ (Fig. 5a,b and Supplementary Fig. 37). Laser beams create a classical diffraction pattern with a series of spots perpendicular to the band alignment (Fig. 5c and Supplementary Fig. 2), matching models with corresponding effective slit size on the order of ~400 nm (Fig. 5d). Linear dichroism (LD) spectroscopy of the thin film with vertically aligned stripes provides a strong LD response, indicating highly linear optical properties (Fig. 5e, red). Following 90° rotation the LD spectrum inverts, becoming a mirror image of the 0° spectrum (Fig. 5e, blue). Linear alignment of oleic acid affects these spectra: signals in LD spectra have a high correlation with the UV-visible (UV-vis) absorption spectrum (Fig. 5e, black) for oleic acid at wavelengths <250 nm. In addition, the thin film exhibits a strong circular dichroism (CD) response and g-factor

(Fig. 5f). Chiroptic properties could emanate from helical features in cables (Fig. 5g).

Conclusions

In this work, we show that nanoscale CdS MSCs can spontaneously self-organize into complex structures at centimetre scales. The multiscale arrangement of MSC building blocks in filaments and striped films presents intriguing analogies to hierarchical assemblies in biological systems. Hierarchical structural organization is pervasive throughout the natural world, and provides a myriad of examples for complex and diverse structure–function relationships. Our work demonstrates the ability of semiconductor nanomaterials to assemble into complex macroscopic structures, which provides a potential platform to realize advanced function.

Online content

Any methods, additional references, Nature Research reporting summaries, source data, extended data, supplementary information, acknowledgements, peer review information; details of author contributions and competing interests; and statements of data and code availability are available at https://doi.org/10.1038/s41563-022-01223-3.

Received: 7 August 2021; Accepted: 21 February 2022; Published online: 14 April 2022

References

- Begley, M. R., Gianola, D. S. & Ray, T. R. Bridging functional nanocomposites to robust macroscale devices. Science 364, eaav4299 (2019).
- Boles, M. A., Engel, M. & Talapin, D. V. Self-assembly of colloidal nanocrystals: from intricate structures to functional materials. *Chem. Rev.* 116, 11220–11289 (2016).
- Liu, Y.-H., Wang, F., Wang, Y., Gibbons, P. C. & Buhro, W. E. Lamellar assembly of cadmium selenide nanoclusters into quantum belts. *J. Am. Chem.* Soc. 133, 17005–17013 (2011).
- Williamson, C. B. et al. Chemically reversible isomerization of inorganic clusters. Science 363, 731–735 (2019).
- Grzelczak, M., Vermant, J., Furst, E. M. & Liz-Marzán, L. M. Directed self-assembly of nanoparticles. ACS Nano 4, 3591–3605 (2010).
- Fan, J. A. et al. Self-assembled plasmonic nanoparticle clusters. Science 328, 1135–1138 (2010).
- Vukusic, P. & Sambles, J. R. Photonic structures in biology. Nature 424, 852–855 (2003).
- 8. Denton, E. Reflectors in fishes. Sci. Am. 224, 64-75. (1971).
- Winfree, E., Liu, F., Wenzler, L. A. & Seeman, N. C. Design and self-assembly of two-dimensional DNA crystals. *Nature* 394, 539–544 (1998).
- Ball, P. The Self-Made Tapestry: Pattern Formation in Nature (Oxford Univ. Press, 2001).
- Szustakiewicz, P. et al. Supramolecular chirality synchronization in thin films of plasmonic nanocomposites. ACS Nano 14, 12918–12928 (2020).
- Jones, A. C. Molecular design of improved precursors for the MOCVD of electroceramic oxides. *J. Mater. Chem.* 12, 2576–2590 (2002).
- Lagerwall, J. P. F. et al. Cellulose nanocrystal-based materials: from liquid crystal self-assembly and glass formation to multifunctional thin films. NPG Asia Mater. 6, e80 (2014).
- Mohammadi, E. et al. Dynamic-template-directed multiscale assembly for large-area coating of highly-aligned conjugated polymer thin films. *Nat. Commun.* 8, 16070 (2017).
- Bangsund, J. S. et al. Formation of aligned periodic patterns during the crystallization of organic semiconductor thin films. *Nat. Mater.* 18, 725–731 (2019).
- Alivisatos, A. P. Perspectives on the physical chemistry of semiconductor nanocrystals. J. Phys. Chem. 100, 13226–13239 (1996).
- Yin, Y. & Alivisatos, A. P. Colloidal nanocrystal synthesis and the organicinorganic interface. *Nature* 437, 664–670 (2005).
- Boneschanscher, M. P. et al. Long-range orientation and atomic attachment of nanocrystals in 2D honeycomb superlattices. Science 344, 1377–1380 (2014).
- Geuchies, J. J. et al. In situ study of the formation mechanism of two-dimensional superlattices from PbSe nanocrystals. *Nat. Mater.* 15, 1248–1254 (2016).
- Alivisatos, A. P. et al. Organization of 'nanocrystal molecules' using DNA. Nature 382, 609–611 (1996).
- Mirkin, C. A., Letsinger, R. L., Mucic, R. C., Storhoff, J. J. & DNA-Based, A. Method for rationally assembling nanoparticles into macroscopic materials. *Nature* 382, 607–609 (1996).

- Wang, S. et al. Colloidal crystal engineering with metal-organic framework nanoparticles and DNA. *Nat. Commun.* 11, 2495 (2020).
- 23. Heuer-Jungemann, A. et al. The role of ligands in the chemical synthesis and applications of inorganic nanoparticles. *Chem. Rev.* **119**, 4819–4880 (2019).
- Nevers, D. R. et al. Mesophase formation stabilizes high-purity magic-sized clusters. J. Am. Chem. Soc. 140, 3652–3662 (2018).
- Baek, W. et al. Highly luminescent and catalytically active suprastructures of magic-sized semiconductor nanoclusters. Nat. Mater. 20, 650–657 (2021).
- Nevers, D. R., Williamson, C. B., Hanrath, T. & Robinson, R. D. Surface chemistry of cadmium sulfide magic-sized clusters: a window into ligandnanoparticle interactions. *Chem. Commun.* 53, 2866–2869 (2017).
- 27. Zhu, C., Lu, Y., Jiang, L. & Yu, Y. Liquid crystal soft actuators and robots toward mixed reality. *Adv. Funct. Mater.* 31, 2009835 (2021).
- Bishop, K. J. M., Wilmer, C. E., Soh, S. & Grzybowski, B. A. Nanoscale forces and their uses in self-assembly. Small 5, 1600–1630 (2009).
- Schapotschnikow, P. & Vlugt, T. J. H. Understanding interactions between capped nanocrystals: three-body and chain packing effects. *J. Chem. Phys.* 131, 124705 (2009).
- Tan, S. F., Chee, S. W., Lin, G. & Mirsaidov, U. Direct observation of interactions between nanoparticles and nanoparticle self-assembly in solution. *Acc. Chem. Res.* 50, 1303–1312 (2017).
- Blyholder, G., Adhikar, C. & Proctor, A. Structure and orientation of oleic acid adsorbed onto silica gel. *Colloids Surf. A* 105, 151–158 (1995).
- Kumar, A. & Molinero, V. Self-assembly of mesophases from nanoparticles. J. Phys. Chem. Lett. 8, 5053–5058 (2017).

- Viney, C. & Putnam, W. S. The banded microstructure of sheared liquid-crystalline polymers. *Polymer* 36, 1731–1741 (1995).
- Hamdi, R., Petriashvili, G., De Santo, M. P., Lombardo, G. & Barberi, R. Electrically controlled 1D and 2D cholesteric liquid crystal gratings. *Mol. Cryst. Liq. Cryst.* 553, 97–102 (2012).
- Godinho, M. H., Fonseca, J. G., Ribeiro, A. C., Melo, L. V. & Brogueira, P. Atomic force microscopy study of hydroxypropylcellulose films prepared from liquid crystalline aqueous solutions. *Macromolecules* 35, 5932–5936 (2002).
- Chung, W.-J. et al. Biomimetic self-templating supramolecular structures. Nature 478, 364–368 (2011).
- Kim, S. H., Misner, M. J., Xu, T., Kimura, M. & Russell, T. P. Highly oriented and ordered arrays from block copolymers via solvent evaporation. *Adv. Mater.* 16, 226–231 (2004).
- Grason, G. M. & Bruinsma, R. F. Chirality and equilibrium biopolymer bundles. *Phys. Rev. Lett.* 99, 098101 (2007).
- Grason, G. M. Braided bundles and compact coils: the structure and thermodynamics of hexagonally packed chiral filament assemblies. *Phys. Rev.* E 79, 041919 (2009).

Publisher's note Springer Nature remains neutral with regard to jurisdictional claims in published maps and institutional affiliations.

© The Author(s), under exclusive licence to Springer Nature Limited 2022

Methods

Materials. The following chemicals were used as received. Oleic acid (90%), cadmium oxide (99.5%), ethyl acetate (≥99.5%), tri-n-octylphsosphine (TOP, 97%), 1-octadecene (ODE, 90%), sulfur (purified by sublimation, particle size ~100 mesh) and hexane (95%, anhydrous) were purchased from Sigma-Aldrich. Methanol (99.8%, certified ACS) was purchased from Fisher Scientific.

Synthetic methods. Preparation of 1.0 M cadmium oleate. In a 50 ml round-bottom flask (RBF) connected to a Schlenk line, 1.28 g (10 mmol) of cadmium oleate (CdOl) and 10 ml (8.95 g) of oleic acid are added. The contents are heated to 50 °C and mixed with a stir bar at 800 r.p.m. At 50 °C the suspended mixture was placed under vacuum and degassed. When fluid bubbling had stopped, the RBF was placed under N2 gas and heated to 140 °C. Around 11 his required for CdOl, at 140 °C, to react completely with oleic acid, and this results in a translucent and viscous tan–orange solution. Once fully reacted, the solution was cooled to 105 °C when the mixture was placed under vacuum to remove water produced by the reaction. When bubbling had subsided, the flask was cooled to 50 °C and placed under $\rm N_2$ gas.

Preparation of $2.5\,M$ TOP sulfur. In an 8 ml scintillation vial in a glovebox, $0.16\,\mathrm{g}$ ($0.005\,\mathrm{mmol}$) of elemental sulfur and $2.0\,\mathrm{ml}$ of TOP were added and the contents mixed with a 1 cm stir bar at $800\,\mathrm{r.p.m.}$ Once fully dissolved, the vial was removed from the glovebox and was air stable. Gentle heating may be required to facilitate the solution of sulfur.

Preparation of CdS MSCs. High-quality CdS MSCs were prepared by the synthetic procedure reported previously²⁴. While the CdOl solution was maintained at 50 °C, 2.0 ml of 2.5 M TOP sulfur solution was injected into 10 ml of 1.0 M CdOl solution. The solution was mixed for 5 min to ensure a homogenous concentration. At this point the mixture can be stored in air by cooling to room temperature and used at any time. The solution was then heated to 140 °C over a 20 min period. Once the temperature had reached 140 °C, the mixture reacted for 60 min. Thereafter, the reaction was cooled to 60 °C and then quenched with 12 ml of ethyl acetate, which produced a white precipitate. The resultant mixtures were transferred to a 45 ml centrifuge tube and spun at 4,400 r.p.m. for 5 min. The supernatant was discarded and the precipitate suspended in hexane (~10 ml). During resuspension the solution gelled substantially. Once fully dissolved, the product was again precipitated with ethyl acetate (~10 ml) and centrifuged for 5 min at 4,400 r.p.m. The supernatant was discarded and the sample dried under vacuum for 24 h.

This synthesis yielded atomically uniform 1.5 nm CdS nanoclusters capped with oleate ligands that rendered the MSC soluble in non-polar organic solvents such as hexane. These nanoclusters feature a molecular structure, successfully modelled in our previous report, through X-ray total scattering and pair distribution function analysis.

Preparation of oleic acid-capped CdOl nanoclusters. A 0.05 M cadmium oleate precursor was prepared by heating a mixture of 0.69 g (5.4 mmol) of CdOl, 8 ml (25.2 mmol) of oleic acid and 92 ml of ODE to 250 °C under $\rm N_2$ flow. The CdOl precursor was exposed to $\rm O_2$ at 250 °C for 10 min when the colour of the solution slowly turned light brown, indicating the formation of CdOl nanoclusters. The final product was precipitated with 200 ml of acetone and isolated following centrifugation.

Preparation of oleic acid-capped CdS nanoparticles. The synthesis of CdS nanoparticles is adapted from previous works by Peng et al. and our group 26,40 . In a typical synthesis, 0.69 g (5.4 mmol) of CdOl, 8 ml (25.2 mmol) of oleic acid and 92 ml of ODE were mixed in a 250 ml round-bottom flask and heated to 300 °C under $\rm N_2$ flow, resulting in a colourless solution containing 0.05 M CdOl in ODE. The sulfur source was prepared by dissolving 30 mg (0.9 mmol) of elemental sulfur in 3 ml of ODE. The solution was loaded into a 5 ml syringe and rapidly injected into the CdOl solution at 300 °C. After 3 min the reaction mixture became bright yellow and was quickly cooled to room temperature, from which CdS nanoparticles were precipitated with 200 ml of acetone and isolated following centrifugation.

Preparation of thin films. High-quality CdS MSC solids were dissolved in hexanes to create colourless, transparent solutions of varying concentration (5, 10, 20, 40 and 100 mg ml $^{-1}$). MSC solution (50 µl) was drop-cast onto a glass slide to which three sides of Scotch tape had been preattached, as shown in Supplementary Fig. 1. Next, another glass slide was carefully placed on top of the Scotch tape. The MSC solution should not touch the Scotch tape, otherwise the thin film would not be aligned parallel to the evaporation front. The thickness of the Scotch tape used here was about $100\,\mu\text{m}$. The setup shown in Supplementary Fig. 1 resulted in thin films with linearly aligned fibres. The evaporation rate can be effectively tuned by placing the glass slides in a container either saturated with hexane vapour or under a slight vacuum. In addition, because it was found that patterning of the thin film is highly dependent on the concentration of the MSC solution, different concentrations (10, 15, 20, 40 and 100 mg ml $^{-1}$) of MSC solution were used for the preparation of thin films. Sonication of the MSC mother solution for 10 min effectively disentangled the assembled structures.

Characterization methods. *UV-vis absorption spectroscopy.* Measurements of thin films were performed on a Cary-5000 spectrometer at a spectral resolution of 0.5 nm.

CD and LD spectroscopy. Measurements were performed on a JASCO-1500 spectropolarimeter at room temperature, with sensitivity, time constant and scan rate chosen appropriately. The corresponding high-tension and absorption spectra were also monitored during the measurement process. In general, CD and LD signals were collected simultaneously in the wavelength range 200–500 nm, with an interval of 0.5 nm and a scanning speed of 50 nm min⁻¹.

POM. POM images were acquired on an Olympus BX51 optical microscope. Regular OM images were acquired by setting the polarizer and analyser parallel with each other, while POM images were taken with the polarizer and analyser perpendicular to each other.

AFM. AFM images were taken on an Asylum-MFP3D-Bio atomic force microscope.

LSCM. LSCM images were taken on a Keyence VK-X260 3D laser scanning confocal microscope. The thin film was prepared from $20\,mg\,ml^{-1}$ MSC solution, and a representative region of $290\times200\,\mu m^2$ was investigated by LSCM. The glass substrate was used as the reference surface

SEM. The thin film was first coated with a conductive carbon layer and the surfactant texture imaged on a Zeiss Gemini 500 scanning electron microscope.

TEM. TEM images were acquired on a FEI Tecnai T12 transmission electron microscope operating at 120 kV with a LaB6 tip. Samples for TEM analysis were prepared by placing a drop of 1 mg ml $^{-1}$ MSC solution onto a copper grid coated with an amorphous carbon film.

High-resolution STEM. STEM images were acquired using an aberration-corrected FEI Titan Themis operating at 300 kV, with a convergence semi-angle of 30 mrad and inner and outer collection angles of 68 and 340 mrad, respectively, on an annular dark-field detector. Samples were prepared by drop-casting a solution of MSCs in hexane on a standard carbon-coated Cu-TEM grid. The grids were then placed on a hot plate at 60 °C and under vacuum to ensure that solvent was removed before imaging.

Laser diffraction. For the transmission experiment, we passed a laser through our film and studied the diffraction patterns formed (Supplementary Fig. 2). We used a green laser of 532 nm wavelength and a violet of 405 nm for the experiment, and fixed the position of the laser relative to the film while maintaining the distance of the film from the detector/observer screen at 25 cm for consistency.

Theoretical calculations. The magnitude for static and instantaneous dipolar moment were calculated through density functional theory (DFT), with molecular dynamics for thermal vibrations (25 ps timeframe). DFT calculations were performed using the SIESTA open-source DFT package. Perdew–Burke–Ernzerhoff functional within generalized gradient approximation, Troullier–Martins pseudo-potentials, 400-Ry real-space grid cutoff and a triple-zeta plus polarization basis set were used throughout. To achieve perfect passivation, pseudo-hydrogens with 0.5 and 1.5 charges were used, as implemented in SIESTA, and formate or halide ligands for a more realistic passivation.

Reporting summary. The preparation conditions for all thin films investigated in this work are summarized in Supplementary Table 1.

Data availability

The data supporting the findings of this study are available within the paper, and other findings of this study are available from the corresponding authors upon reasonable request.

References

 Yu, W. W. & Peng, X. Formation of high-quality CdS and other II–VI semiconductor nanocrystals in noncoordinating solvents: tunable reactivity of monomers. Angew. Chem. Int. Ed. Engl. 41, 2368–2371 (2002).

Acknowledgements

This work was supported in part by the National Science Foundation (NSF) under award numbers CHE-1507753, CHE-2003586, CMMI-1941135, CHE-1665305 and DMR-1809429. Electron microscopy was supported by the NSF under award number DMR-1654596. This work was partially supported by the Cornell Center for Materials Research and made use of the Cornell Center for Materials Research shared facilities, with funding from the the NSF MRSEC programme (number DMR-1719875). R.S.S. acknowledges financial support from the NSF Graduate Research Fellowship Programme under grant

no. DGE-1650441. From the Department of Chemical and Biomolecular Engineering at Cornell University, we thank Y. Cheng for AFM analysis and K. Niccum and M. Johnson for their pioneering work.

Author contributions

H.H. and S.K. synthesized high-quality MSCs and thin films used in the main studies. H.H., S.K., C.B.W. and D.R.N. performed OM and POM. H.H. performed atomic force microscopy, scanning electron microscopy and UV-vis absorption spectroscopy. S.K. conducted laser diffraction experiments, simulations, and optical analysis. H.H. and Y.Y. measured circular and L.D spectroscopy and carried out TEM imaging. B.H.S. and L.E.K. carried out high-resolution STEM. R.S.S. and J.D. contributed to the modelling and understanding of how the strain energy of twisting leads to monodisperse cable thickness. M.X. synthesized and prepared thin films from CdOl nanoclusters and CdS nanoparticles. O.V. calculated dipoles and dipole–dipole interactions between MSCs. S.J.W. contributed the theoretical model for the self-assembly mechanism. R.D.R. and T.H. conceived this project, supervised and guided the design, analysis and interpretation

and wrote the manuscript. All authors contributed to the interpretation of results and preparation of the manuscript.

Competing interests

The authors declare no competing interests.

Additional information

 $\label{thm:continuous} \textbf{Supplementary information} \ The online version contains supplementary material available at $$https://doi.org/10.1038/s41563-022-01223-3.$

Correspondence and requests for materials should be addressed to Tobias Hanrath or Richard D. Robinson.

Peer review information *Nature Materials* thanks the anonymous reviewers for their contribution to the peer review of this work.

Reprints and permissions information is available at www.nature.com/reprints.